Investigating the differences in calculating global mean surface CO_2 abundance: the impact of analysis methodologies and site selection

Zhendong Wu[1,2,*], Alex Vermeulen[2,*], Yousuke Sawa[3], Ute Karstens[1,2], Wouter Peters[4,5], Remco de Kok[4], Xin Lan[6,7], Yasuyuki Nagai[3], Akinori Ogi[3], Oksana Tarasova[8]

[1]ICOS Carbon Portal at Lund University, Department of Physical Geography and Ecosystem Sciences, Lund, Sweden
[2]ICOS ERIC, Carbon Portal, Lund, Sweden
[3]Japan Meteorological Agency (JMA), Tokyo, Japan
[4]Wageningen University, Wageningen, The Netherlands
[5]University of Groningen, Groningen, The Netherlands
[6]NOAA Global Monitoring Laboratory (GML), Boulder, USA
[7]Cooperative Institute for Research in Environmental Sciences, University of Colorado Boulder, USA
[8]WMO, Geneva, Switzerland

Correspondence to: Alex Vermeulen (alex.vermeulen@icos-ri.eu), and Zhendong Wu (zhendong.wu@nateko.lu.se)

Abstract. The World Meteorological Organization (WMO) Global Atmosphere Watch (GAW) coordinates high-quality atmospheric greenhouse gas observations globally and provides these observations through the WMO World Data Centre for Greenhouse Gases (WDCGG) supported by Japan Meteorological Agency. The WDCGG and the National Oceanic and Atmospheric Administration (NOAA) analyse these measurements using different methodologies and site selection to calculate global annual mean surface CO_2 and its growth rate as a headline climate indicator. This study proposes a third hybrid method named semi-NOAA, which is used as an independent validation of the methods as described by NOAA and WDCGG. We apply the semi-NOAA to incorporate observations from most WMO GAW stations and 3D modelled CO_2 fields from CarbonTracker Europe (CTE). We found that different observational networks (i.e., the NOAA, GAW, and CTE networks) and analysis methods result in differences in the calculated global surface CO_2 mole fractions equivalent to the current atmospheric growth rate over a three-month period. However, the CO_2 growth rate derived from these networks and CTE model output shows good agreement. Over the long-term period (40 years), both networks with and without continental sites exhibit the same trend in the growth rate (0.030 ± 0.002 ppm per year). However, a clear difference emerges in the short-term (one month) change of the growth rate. The network that includes continental sites improves the early detection of changes in biogenic emissions.

1 Introduction

Global mean surface temperature averaged over 2011-2020 has increased by about 1.09°C relative to the average temperature of 1850–1900 (Gulev et al., 2021). The increasing amount of atmospheric carbon dioxide (CO_2), together with increases in other greenhouse gases, is the main driver of the warming (Eyring et al., 2021). After being relatively stable between 180 ppm (ice age) and 280 ppm (interglacial) for the last 800,000 years (Lüthi et al., 2008), the annual average CO_2 level of the atmosphere has increased since the industrial revolution from roughly 277 ppm in 1750 to 415.7±0.2 ppm in 2021 (WMO, 2022), due to emissions of CO_2 related to human activities like burning of fossil fuels and land use changes (Friedlingstein et al., 2022). Mean global atmospheric CO_2 annual growth rate (G_{ATM}) is an important constraint on the global carbon cycle. Based on the most recent Global Carbon Budget (GCB) analysis (Friedlingstein et al., 2022), the total emission of CO_2 due to human activities was 10.2 ± 0.8 GtC yr^{-1} in 2020, of which 3.0 ± 0.4 GtC yr^{-1} was captured by the ocean sink and 2.9 ± 1 GtC yr^{-1} by the terrestrial sink, leaving a net increase of 5.0 ± 0.2 GtC yr^{-1} of CO_2 in the atmosphere, corresponding to an atmospheric CO_2 mole fraction increase of 2.4 ± 0.1 ppm yr^{-1}.

As the atmosphere mixes the contributions of all sources and sinks, an observational global average CO_2 mole fraction can be constructed if there are enough observations to represent the spatial and temporal variation across the globe. Since most land masses are concentrated in the Northern Hemisphere, and the highest anthropogenic emissions (e.g. during winter) occur in the relatively narrow latitudinal band between 30 ºN and 60 ºN, relatively large spatial and temporal gradients in CO_2 mole fraction exist in and around that region. Due to convective and advective mixing, the average mixing time of air within the same latitudinal bands varies from several weeks to a month. However, mixing between latitudinal bands is slower, especially the exchange between the northern and southern hemispheres, which has an approximate interhemispheric transport time of 1.4 ± 0.2 years (Patra et al., 2011). The interplay of the latitudinal and interhemispheric differences in fossil fuel emissions and seasonal exchange with land biota (Denning et al., 1995) creates a latitudinal and interhemispheric gradient that requires a sufficiently dense network to capture a representative global annual mean.

However, measurement stations that are close to sources or sinks may not be representative of a large atmosphere volume and the average signal at their latitude. Therefore, inclusion of these observations might introduce significant biases on the global mean CO_2 and its growth rate. These biases can be avoided by filtering of data and a careful selection of spatially representative stations, as done by NOAA in their use of 43 stations (Fig. 1) that are considered to be representative for the Marine Boundary Layer (MBL reference network, https://www.esrl.noaa.gov/gmd/ccgg/mbl/mbl.html). An additional data processing step developed by NOAA to further avoid biases due to unrepresentative local signals is filtering and smoothing, by using a combination of a low pass filter and decomposition into a fitted long-term trend and seasonal cycle (Thoning et al., 1989), hereafter refered to as the NOAA analysis. These fits can also be used to fill gaps for missing data, though care must be taken to avoid extrapolation errors before and beyond the time covered by the data record of the station. The WMO Global Atmosphere Watch (GAW) World Data Centre for Greenhouse Gases (WDCGG) also publishes global averages mole fraction for CO_2 and the other major greenhouse gases. They use curve fitting and filter methods that are very similar to those developed by NOAA, but WDCGG includes continental locations that are potentially influenced by local sources and sinks (Tsutsumi et al., 2009).

The NOAA MBL observations are all part of the NOAA cooperative global air sampling network and analysed in the same laboratory. All NOAA flask-air observations are traceable to the WMO X2019 CO_2 scale that is maintained by NOAA Global Monitoring Laboratory (GML). In contrast, the WDCGG data originate from multiple independent laboratories (including NOAA GML), that together form a network of hundreds of stations coordinated by WMO GAW. Having a multitude of

76   independent laboratories carries an additional risk of biases due to differences in sampling, measurement, and analysis

77   methods, for example calibration scales, although much care is taken to avoid these by coordination in the network and use of

78   a common calibration scale from the WMO Central Calibration Laboratory (CCL) guided by a set of strict measurement

79   compatibility goals (WMO, 2022). The different selection of stations results in a larger seasonal cycle amplitude in WDCGG

80   results compared to those of NOAA and a small but quite consistent bias in global surface annual mean CO_2 mole fraction

81   (Tsutsumi et al., 2009). The NOAA estimate of global surface annual mean CO_2 mole fraction is expected to be negatively

82   biased (e.g. ~0.35 ppm lower than the WDCGG estimate, Tsutsumi et al., 2009) compared to a full global surface average

83   because areas with large sources are not represented. However, none of the two afore mentioned approaches represents those

84   parts that have the atmosphere with low CO_2 mole fraction levels, i.e. the full troposphere (up to ~8-15 km altitude) and the

85   stratosphere or the regions of the world with substantial observational gaps.

86   In this paper we propose a data integration method to estimate the global mean surface CO_2 and its growth rate, named semi-

87   NOAA, which is used as an independent validation of the methods as described by NOAA and WDCGG through a completely

88   independent and open-source implementation. We apply the semi-NOAA methodology to incorporate CO_2 data from the

89   GAW network (139 stations, Fig. 1) and a well-established 3D global transport model (TM5: Transport Model 5, Peters et al.,

90   2004, Krol et al., 2005). We investigate the influence of small differences between the three methodologies and whether these

91   are significant or not for calculating the global mean surface CO_2 and its growth rate, how consistent the semi-NOAA and

92   WDCGG approaches are with each other, and how they compare with NOAA analysis and estimates derived from a CO_2

93   simulation with the 3D transport model TM5. These 3D CO_2 results for 2001-2020 using TM5 are performed in the

94   CarbonTracker Europe framework (CTE, Peters et al., 2004, Van Der Laan-Luijkx et al., 2017), where the CO_2 uptake and

95   emission fluxes are optimized by the inversion system to minimize the mismatch between the *in situ* observations and the

96   modelled CO_2 mole fraction. CTE generally has a good representation of the CO_2 field, with mean biases with respect to

97   independent aircraft measurements of generally less than 0.5 ppm (Friedlingstein et al., 2022). Furthermore, the inferred CO_2

98   fluxes from CTE fit well within the ensemble of those of other inversions used for the evaluation of Global Carbon Budget

99   (e.g. Friedlingstein et al., 2022).

100 **2 Methods and data**

101
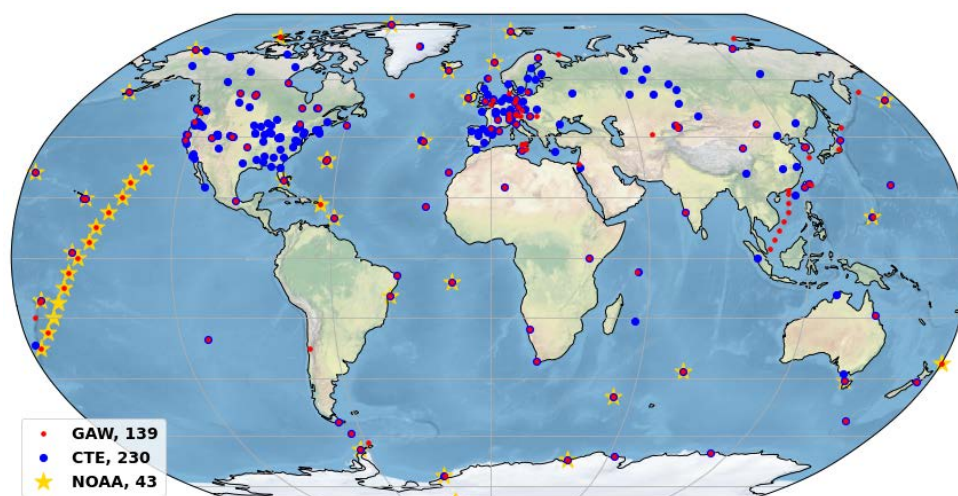
102 **Figure 1. The selected GAW global network for CO_2 measurement (139 sites, red dots), the global network for the**
103 **CTE evaluations (230 sites, blue dots), and the NOAA network (43 sites, yellow stars).**

104 **2.1 The WMO GAW observations and WDCGG analysis method**

105 The WMO GAW network measurements are archived and distributed by WDCGG (World Data Center for Greenhouse Gases),
106 hosted by the Japan Meteorological Agency. The GAW observations used in this study originate from 139 selected stations
107 of the GAW network, and all observations are on the WMO standard scale, WMO-CO_2-X2019 (Hall et al., 2021). The details
108 on the station selection are described in Tsutsumi et al., (2009), which mainly excludes stations located in the northern
109 hemisphere that show large standard deviations from the latitudinal fitted curve. The remaining 139 stations show a more
110 reasonable latitudinal scatter range (Fig. 1).

111 The WDCGG global analysis method (hereafter WDCGG method), as described in Tsutsumi et al., (2009), includes the
112 mentioned station selection, a data fitting and filter (involves data interpolation and extrapolation), and calculation of the zonal
113 and global mean mole fractions, trends, and growth rates. The procedure is also summarized in Text S1.

114 The output from the global analysis by the WDCGG method are used to compare against an alternative method (semi-NOAA)
115 that we designed to follow as closely as possible the fit and filter method (Conway et al., 1994) deployed by NOAA and is
116 described in the section 2.3.

117 **2.2 CTE model output and station observations**

118 CarbonTracker Europe (CTE) is a global model of atmospheric CO_2 and designed to keep track of CO_2 uptake and release at
119 the Earth's surface over time (Van Der Laan-Luijkx et al., 2017). CTE incorporates an off-line atmospheric transport module
120 (TM5, Peters et al., 2004, Krol et al., 2005) driven by ECMWF ERA5 data, and there are four prescribed fluxes (i.e. from
121 ocean, biosphere, fire and fossil fuel), which are transported in the model, together with the transported initial CO_2 field. CTE
122 also includes a data assimilation system that applies an ensemble Kalman filter to optimize the biogenic and ocean fluxes for
123 a combination of plant-functional types and climate zones to improve the fit of the simulated concentrations with observations.

124   The optimized fluxes from the data assimilation have been used in Global Carbon Project (GCP) 2021 (Friedlingstein et al.,

125   2022), and CTE compares well to the other data assimilation systems used in GCP.

126   The CTE model data used here consisted of simulated monthly CO_2 mole fraction at 1x1 degree horizontal resolution and 25

127   levels in the vertical, the data period ranges from 2001 to 2020 which has no influence of model spin-up (Krol et al., 2018).

128   From the CTE output a set of simulated synthetic atmospheric CO_2 mole fractions with monthly resolution can be extracted

129   within grid cells where stations are situated. This study analyses monthly observation data (1980-2020) and synthetic time

130   series (2001-2020) by using the semi-NOAA method (section 2.3) and attempts to estimate global mean CO_2 mole fraction

131   and its growth rate. The observed CO_2 mole fractions are taken from 230 out of 290 global-wide distributed stations (Fig. 1,

132   the station selection is summarized in Text S2), the data come from the GLOBALVIEW-plus ObsPack data product (Kenneth

133   N., 2022), and include surface-based, shipboard-based and tower-based measurements.

2.3 The semi-NOAA method

135   The temporal pattern of CO_2 measurement records at locations around the globe can be explained as the combination of

136   roughly three components: a long-term trend, a non-sinusoidal yearly cycle (or seasonality), and short-term variations. This

137   study synchronizes monthly CO_2 records with the fitting and filter method obtained from the NOAA Global Monitoring

138   Laboratory (Thoning et al., 1989, Conway et al., 1994), without extrapolation. The station selection and CO_2 averaging method

139   are kept the same as in the WDCGG method (Text S1). This method will be referred to as the semi-NOAA method and will

140   be compared to the WDCGG method without extrapolation. The only difference from WDCGG method without extrapolation

141   is the fitting and filter method. All code for the method described here was developed in Python and is available as a Jupyter

142   notebook under a GPL license [https://doi.org/10.18160/Q788-9081]. The semi-NOAA method can be summarized by the

143   following three steps.

2.3.1. Fitting and filter

145   CO_2 records from each station can be abstracted as a combination of long-term trend and seasonality, which can be fitted by

146   a function consisting of polynomial and harmonics. We applied a linear regression analysis based on 3 polynomial coefficients

147   and 4 harmonics (Eq. 1) to fit CO_2 data using general linear least-squares fit (LFIT, Press et al., 1988).

148
$$f(x) = a_0 + a_1 t + a_2 t^2 + \cdots + a_k t^k + \sum_{n=1}^{n_h} (A_n \cos 2\pi nt + B_n \sin 2\pi nt) \qquad (1)$$

149   where a_k, A_n and B_n are fitted parameters, t is the time from the beginning of the observation and it is in months and

150   expressed as a decimal of its year. k denotes polynomial number, $k = 2$. n_h denotes harmonic number, $n_h = 4$. Fig. 2

151   illustrates the function fit to CO_2 data to gain the annual oscillation (red line in Fig. 2a), is a combination of a polynomial fit

152   to the trend (blue line in Fig. 2a) and harmonic fit to the seasonality (green line in Fig. 2b).

153   The residuals are the difference between raw data and the function fit (black dots in Fig. 2c). The filtering method is based on

154   Thoning et al. (1989) which transforms CO_2 data from time domain to frequency domain using a Fast Fourier Transform

155   (FFT), then applies of a low pass filter to the frequency data to remove high-frequency variations, and then transform the

156   filtered data back to the time domain using an inverse FFT. The short term (a cut-off value of 80 days, red line in Fig. 2c) and

157   long term (a cut-off value of 667 days, blue line in Fig. 2c) filters used here are the same as in NOAA method, and applied to

158   obtain the short term and interannual variations that are not determined by the fit function. The original part of the code is also

159   available as Python code from the NOAA website [https://gml.noaa.gov/aftp/user/thoning/ccgcrv/].

2.3.2. Calculate smoothed CO₂ and long-term trend

The results of the filtering residuals are then added to the fitted curve to obtain smoothed CO_2 and its long-term trend. The smoothed CO_2 comprises the fitted trend, the fitted seasonality and the smoothed residuals (red line in Fig. 2d), which only removes short-term variations or noise. The long-term trend comprises fitted trend and residual trend, which removes seasonal cycle and noise (blue line in Fig. 2d).

2.3.3. Calculate CO₂ growth rate, G_ATM

G_{ATM} is determined by taking the first derivative of the long-term trend. However, the growth is made up of discrete points, e.g. the black dots in Fig. 3a shows the trend points. In this case, a cubic spline interpolation is applied to the trend points, in which the spline curve passes through each trend points, as the blue line in Fig. 3a. G_{ATM} is obtained by taking the derivative of the spline at each trend point (Fig. 3b).
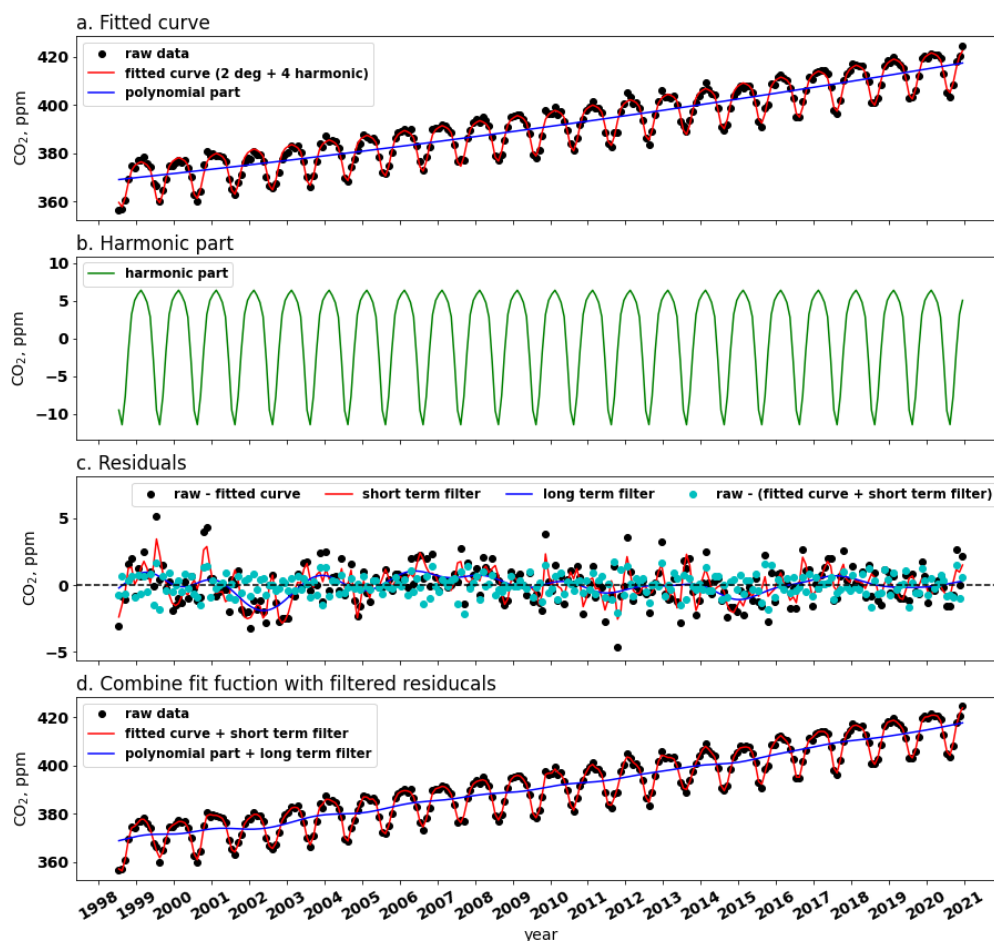
Figure 2. Example of analysed CO₂ data from PAL station (Pallas, Finland), illustrating semi-NOAA curve fitting and filter method. Panel (a) shows monthly averaged CO₂ (dots), curve fitting with 2-degree polynomial and 4-degree harmonics (red line), and long-term trend estimated by a 2-degree polynomial (blue line). Panel (b) shows seasonality estimated by 4-degree harmonics. Panel (c) shows the residuals of raw data from the function fit (black dots), the red

175 **line is obtained by the short-term filter and the blue line is obtained by the long-term filter. The cyan dots show the**
176 **residuals of raw data from the sum of fitted curve and smoothed residuals. Panel (d) shows final processed CO₂, which**
177 **comprises fitted trend, fitted seasonality and smoothed residuals (red line). The blue line shows final trend which**
178 **comprises fitted trend and residuals trend.**
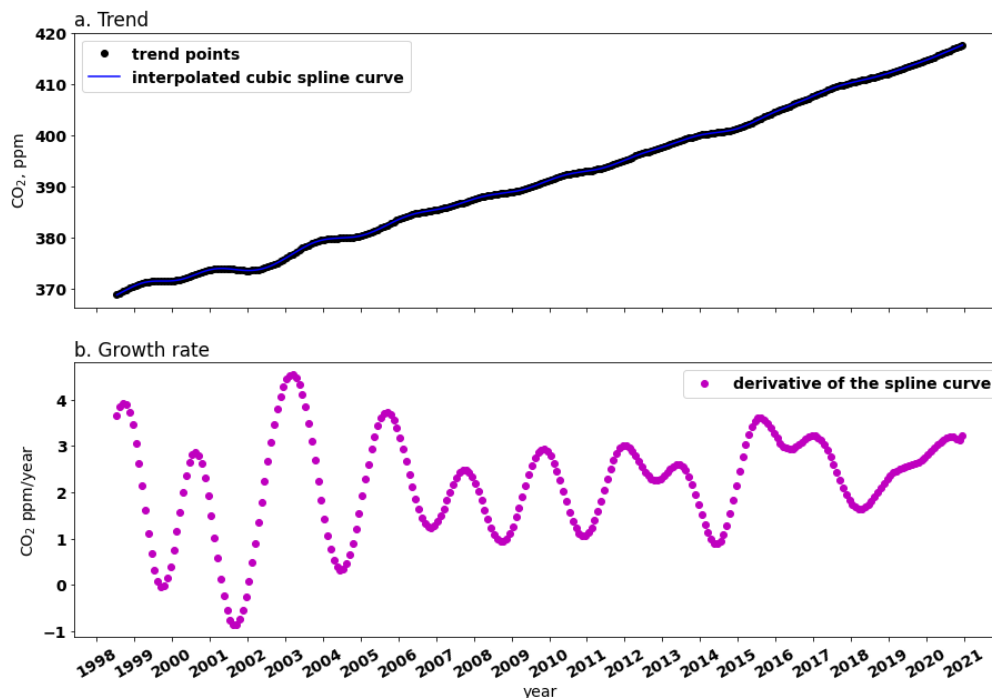
179

180 **Figure 3. Example of CO₂ growth rate, the raw data is the same as used in Fig. 2 from station PAL (Pallas, Finland).**
181 **Panel (a) shows the trend points (black dots) and its cubic spline interpolation (blue line). Panel (b) shows the G_{ATM} at**
182 **each trend point.**

183 **3 Results**

184 Global averaged surface CO₂ and its G_{ATM} are calculated from the GAW observations from 139 sites (Fig. 1) using the

185 WDCGG method with and without extrapolation and our semi-NOAA method, namely GAW (WDCGG+), GAW (WDCGG)

186 and GAW (semi-NOAA). The semi-NOAA method is also applied to three CTE datasets: 1) observations from 230 sites

187 selected in the CTE dataset (hereafter these sites are named as CTE network, Fig. 1) which comes from the ObsPack data

188 product (Kenneth N., 2022), namely CTE_obs (semi-NOAA); 2) CTE model output at the sites (sampled at the same location,

189 altitude and time), namely CTE_output (semi-NOAA); and 3) model output for full global grids (averaged over the first three

190 levels, 0 to 0.35 km Alt.), namely CTE_global (semi-NOAA). We calculated the global means and its G_{ATM} by area-weighted

191 averaging the zonal means over each latitudinal band (30°), as same as the CO₂ averaging method in Tsutsumi et al. (2009).

192 A bootstrap method is used to estimate the uncertainties of global CO₂ mean and its G_{ATM}, which is an almost identical

193 uncertainty analysis as presented by Conway et al. (1994) who constructed 100 bootstrap networks for the NOAA analysis.

194 We construct 200 bootstrap networks which is consistent with the WDCGG analysis in Tsutsumi et al., (2009). For each

195 bootstrap network, we randomly draw the same number of sites (as the actual network, e.g. 139 sites for GAW network) with

196 replacement (or restitution) from the actual network, which means some sites are missing whereas others will be represented

197 twice or more often. We calculate global mean CO_2 mole fraction and its G_{ATM} for each network, and then calculate the

198 statistics (i.e. mean and 68% confidence interval, CI) on the 200 networks. All uncertainties in this paper are reported as ±

199 68% CI.

3.1 Globally averaged surface CO_2 mole fraction and its G_{ATM}

201
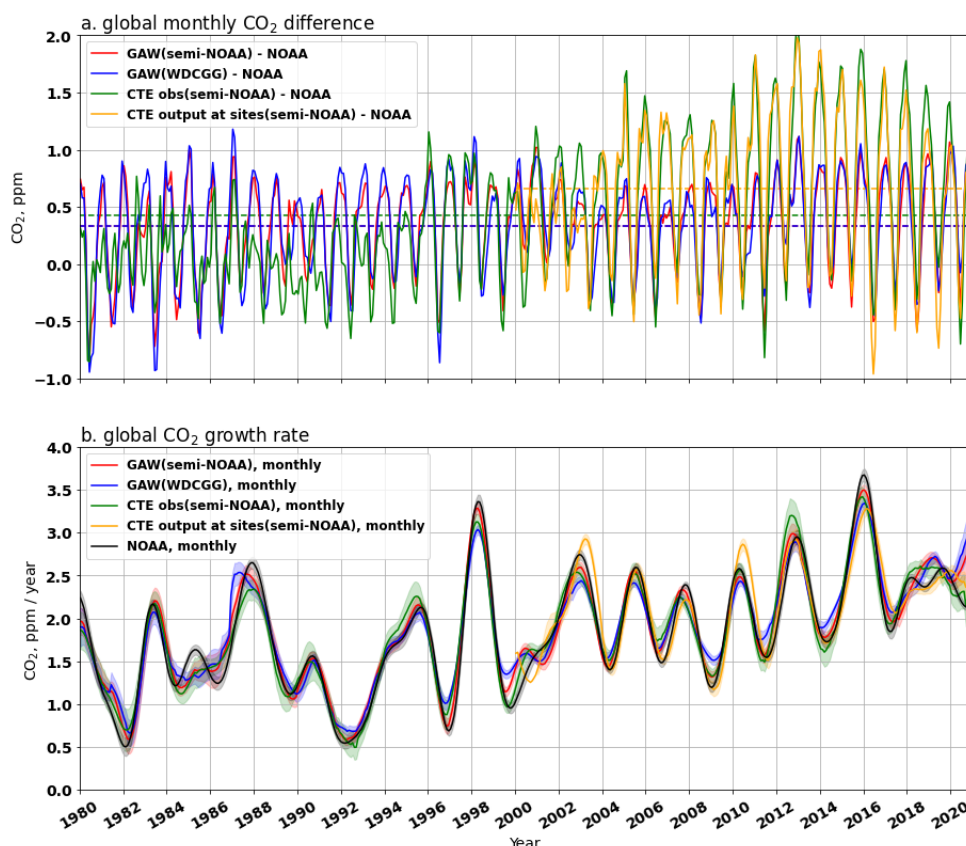
Figure 4. Comparison of globally averaged CO_2 mole fraction (a) and its G_{ATM} (b) from 1980 to 2020. Panel (a) shows the global monthly CO_2 mole fraction from 139 GAW sites (estimated from observations only) and those from 230 sites used in CTE (either from observations or model output) differs from NOAA estimates based on 43 MBL sites. Red and blue lines show the CO_2 derived from the GAW observations using semi-NOAA and WDCGG method without extrapolation, respectively. Green and orange lines show the CO_2 derived from observations and model output at the 230 sites assimilated by CTE using semi-NOAA method, respectively. The dash lines show the mean over the available period. Panel (b) compares the global CO_2 growth rate derived from GAW observations using semi-NOAA (red line) and WDCGG method without extrapolation (blue line), CTE observations (green line) and model output (orange line) using semi-NOAA method, and the NOAA analysis (black line). The shadow area shows the uncertainty as 68% confidence interval obtained by the bootstrap analysis.

212 Global averaged surface CO_2 mole fraction derived from the GAW network (GAW (semi-NOAA) or GAW (WDCGG)) is

213 0.329 or 0.336 ppm significantly ($p<0.05$) higher than the NOAA analysis during 1980-2020 (red or blue line in Fig. 4a, Table

214 S1a-b), this result is consistent with Tsutsumi et al., (2009) who found a 0.350 ppm higher global average in the GAW network

215 during 1983-2006. The higher estimate from the GAW network can be explained by inclusion of more diverse sites, not only

216 NOAA's MBL sites, but also more continental sites (Fig. 1). Both global CO_2 and its G_{ATM} derived from the GAW (semi-

217 NOAA) and GAW (WDCGG) are nearly overlapping (the red and blue lines) in Fig. 4a and 4b (as can also be seen by

218 comparing Fig. S1 and S2). The statistic metrics (Table S1a) show high agreement (r=0.999, RMSE=0.053 ppm, ME=0.007

219 ppm for the CO_2 mole fraction; r=0.991, RMSE=0.081 ppm yr^{-1}, ME=0.005 ppm yr^{-1} for the G_{ATM}) between these two

220 methods, which confirms that the semi-NOAA method agrees well with WDCGG method without extrapolation. The

221 WDCGG method with extrapolation (i.e. GAW (WDCGG+)), where the long-term trend of each station is extrapolated to the

222 most long-running station period and added to its average seasonal variation to synchronize data period of all stations

223 (Tsutsumi et al., 2009), produces ~0.096 ppm significantly (p<0.05) higher values than the global surface CO_2 mole fraction

224 derived from the GAW (WDCGG) during the common period 1984-2020 (see Table S2), while the extrapolation has tiny

225 effect (RMSE=0.062 ppm yr^{-1}, ME=-0.011 ppm yr^{-1}, Table S2) on the CO_2 growth rate.

226 Global averaged surface CO_2 derived from CTE_obs (semi-NOAA) and CTE_output (semi-NOAA) are 0.422 ppm (1980-

227 2020) and 0.656 ppm (2001-2020) significantly (p<0.05) higher compared to the NOAA analysis, respectively (green and

228 orange lines in Fig. 4a). Comparing the global mean of CTE_obs (semi-NOAA) with CTE_output (semi-NOAA) during the

229 common period 2001-2020, we find a low bias (0.069 ppm in CTE_output, Table S1d-e and Table S3), which indicates that

230 the CTE model results can reproduce the global mean CO_2 levels reasonably well. The global annual CO_2 mole fraction from

231 CTE_obs (semi-NOAA), CTE_output (semi-NOAA) and CTE_global (semi-NOAA) is 0.368 (2001-2020), 0.299 (2001-

232 2020) and 0.186 (2001-2020) ppm significantly (p<0.05) higher than the result of the GAW (semi-NOAA), respectively (Table

233 S1d-f). The higher global mean from CTE_obs (semi-NOAA) and CTE_output (semi-NOAA) is mainly due to more sites in

234 the Northern Hemisphere in the CTE network compared to the GAW network. The lower bias between GAW (semi-NOAA)

235 and CTE_global (semi-NOAA) indicates that the GAW network provides a good representation of the low-level atmosphere

236 (i.e. 0 to 0.35 km altitude) at global scale (Table S1f), or the CTE model has a good performance in the low-level atmosphere.
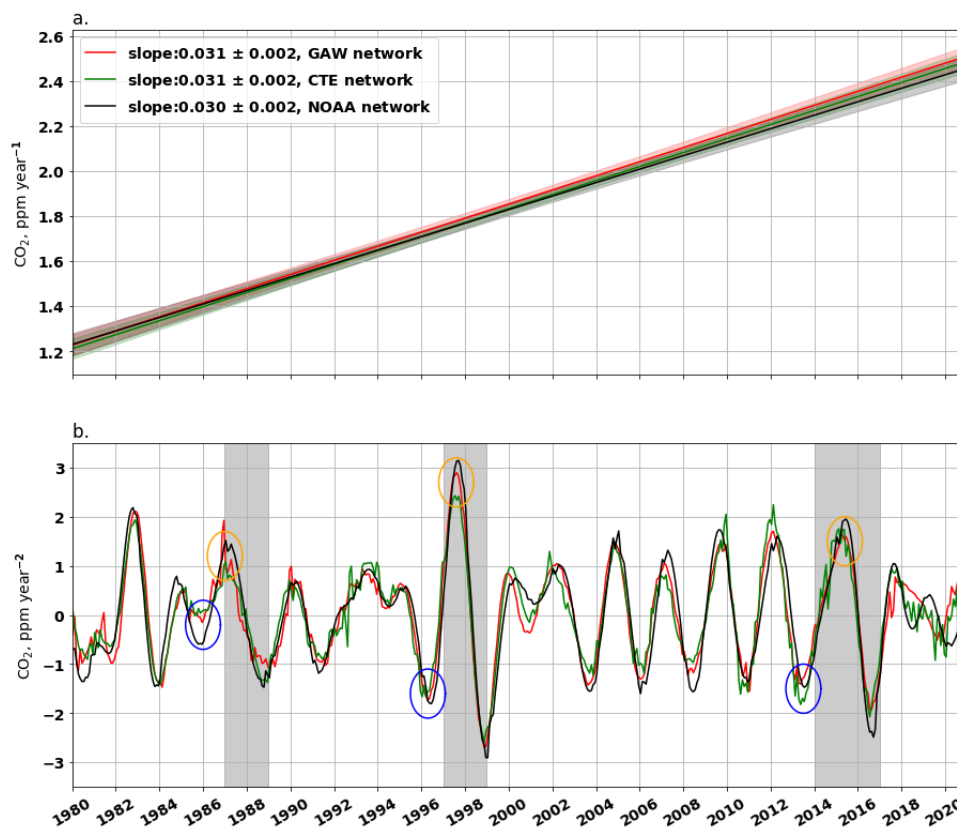
Figure 5. Trend analysis of the global CO₂ growth rate from 1980 to 2020. Panel (a) shows the trends of CO₂ growth rate for the GAW network (red line), the CTE network (green line) and the NOAA network (black line) during the whole period 1980-2020, the CO₂ growth rate is derived from GAW (semi-NOAA), CTE_obs (semi-NOAA) and NOAA analysis (Fig. 4b). Panel (b) shows the trend of CO₂ growth rate for each month during 1980-2020, calculated as the derivative of the growth rate. The grey bands mark the period of three strong El Niño events, i.e 1987-1988, 1997-1998 and 2014-2016.

Despite differences in the global averaged surface CO_2 mole fractions derived from different networks and analysis methods, the G_{ATM} derived from GAW network, CTE network and its model output, and NOAA network agree well (r>0.903, RMSE<0.192 ppm yr⁻¹, MAE<0.158 ppm yr⁻¹, ME<0.025 ppm yr⁻¹, Table S1) during the common period (Fig. 4b). The trend analysis shows that the G_{ATM} increased steadily (0.030 ± 0.002 ppm per year each year) from 1980 to 2020 (Fig. 5a) based on the observations from the three networks (i.e. GAW, CTE and NOAA). This implies that over long-term period (here 40 years) the networks with and without continental sites show the same trend of the G_{ATM}. Hence, the CO_2 advective transport and mixing plays a negligible role in estimating the long-term change of the G_{ATM}. However, there is a clear difference in the short-term (here one month) change of the G_{ATM} between the networks with and without continental sites (Fig. 5b). The El Niño event often diminishes net global C uptake (due to e.g. droughts, floods and fires) and increases global CO_2 growth rate (Sarmiento et al., 2010). The G_{ATM} derived from the GAW and CTE network (red and blue lines) increases earlier before the three strong El Niño events (marked as blue circles in Fig. 5b) and reaches the peak earlier during the El Niño events (marked as orange circles in Fig. 5b), compared to the G_{ATM} derived from the NOAA network (black line). This indicates that continental sites can help early detection of the change of G_{ATM} which is caused by biogenic emission or uptake changes. The

257 CTE network (green line) detects the change even earlier than the GAW network (red line) for the three El Niño events (Fig.

258 5b), which is due to even more continental sites included in the CTE network (Fig. 1), although the more continental sites also

259 induce the larger variability.

260 Table 1 shows the global annual CO_2 and its G_{ATM} derived from GAW (semi-NOAA), together with the uncertainty estimated

261 by the bootstrap method. The global average surface CO_2 mole fraction has increased from 339.17±0.38 ppm in 1980 to

262 413.06±0.16 ppm in 2020 (Table 1, Fig. S1). The uncertainty before 1990 is larger than after 1990, due to fewer measurement

263 stations over the globe before 1990. The average G_{ATM} for the two decades before 2000 is about 1.54±0.08 ppm yr^{-1}, however,

264 in the following two decades it increases to 1.91±0.05 ppm yr^{-1} (2000-2009) and 2.41±0.06 ppm yr^{-1} (2010-2019) (Table 1,

265 Fig. S1).

266 **Table 1. Annual global averaged CO_2 mole fraction (Mean, ppm) and its G_{ATM} (ppm yr^{-1}) derived from GAW**
267 **observations using semi-NOAA method. U(Mean) and U(G_{ATM}) respectively indicate the uncertainty of Mean and its**
268 **G_{ATM} as 68% confidence interval. The annual value is averaged over the monthly values of the year.**

Year	1980	1981	1982	1983	1984	1985	1986	1987	1988	1989
Mean	339.17	340.16	341.03	342.59	344.46	345.69	347.08	348.99	351.45	353.15
U(Mean)	0.38	0.24	0.19	0.24	0.26	0.22	0.14	0.15	0.12	0.15
G_{ATM}	1.65	1.07	0.88	2.02	1.32	1.38	1.55	2.38	2.08	1.23
U(G_{ATM})	0.12	0.10	0.15	0.13	0.08	0.11	0.14	0.08	0.09	0.06
Year	**1990**	**1991**	**1992**	**1993**	**1994**	**1995**	**1996**	**1997**	**1998**	**1999**
Mean	354.22	355.64	356.37	357.09	358.51	360.52	362.27	363.40	366.14	368.10
U(Mean)	0.10	0.11	0.10	0.10	0.11	0.12	0.12	0.10	0.10	0.10
G_{ATM}	1.41	1.03	0.65	1.22	1.72	2.06	1.16	1.82	2.89	1.34
U(G_{ATM})	0.08	0.06	0.05	0.05	0.05	0.08	0.07	0.05	0.05	0.05
Year	**2000**	**2001**	**2002**	**2003**	**2004**	**2005**	**2006**	**2007**	**2008**	**2009**
Mean	369.30	370.77	372.92	375.45	377.22	379.28	381.38	383.20	385.26	386.78
U(Mean)	0.12	0.11	0.10	0.10	0.10	0.10	0.09	0.10	0.10	0.11
G_{ATM}	1.58	1.58	2.33	2.17	1.66	2.42	1.75	2.20	1.71	1.68
U(G_{ATM})	0.05	0.06	0.06	0.04	0.04	0.03	0.05	0.04	0.05	0.04
Year	**2010**	**2011**	**2012**	**2013**	**2014**	**2015**	**2016**	**2017**	**2018**	**2019**
Mean	389.01	390.97	393.14	396.00	397.79	400.12	403.47	405.70	407.93	410.57
U(Mean)	0.12	0.12	0.14	0.11	0.10	0.10	0.11	0.09	0.10	0.13
G_{ATM}	2.32	1.73	2.74	2.30	1.91	2.98	2.95	2.04	2.50	2.61
U(G_{ATM})	0.05	0.06	0.09	0.05	0.04	0.05	0.06	0.06	0.07	0.05
Year	**2020**									
Mean	413.06									
U(Mean)	0.16									
G_{ATM}	2.60									
U(G_{ATM})	0.16									

269   **3.2 Vertical profile of global CO₂ mole fraction**
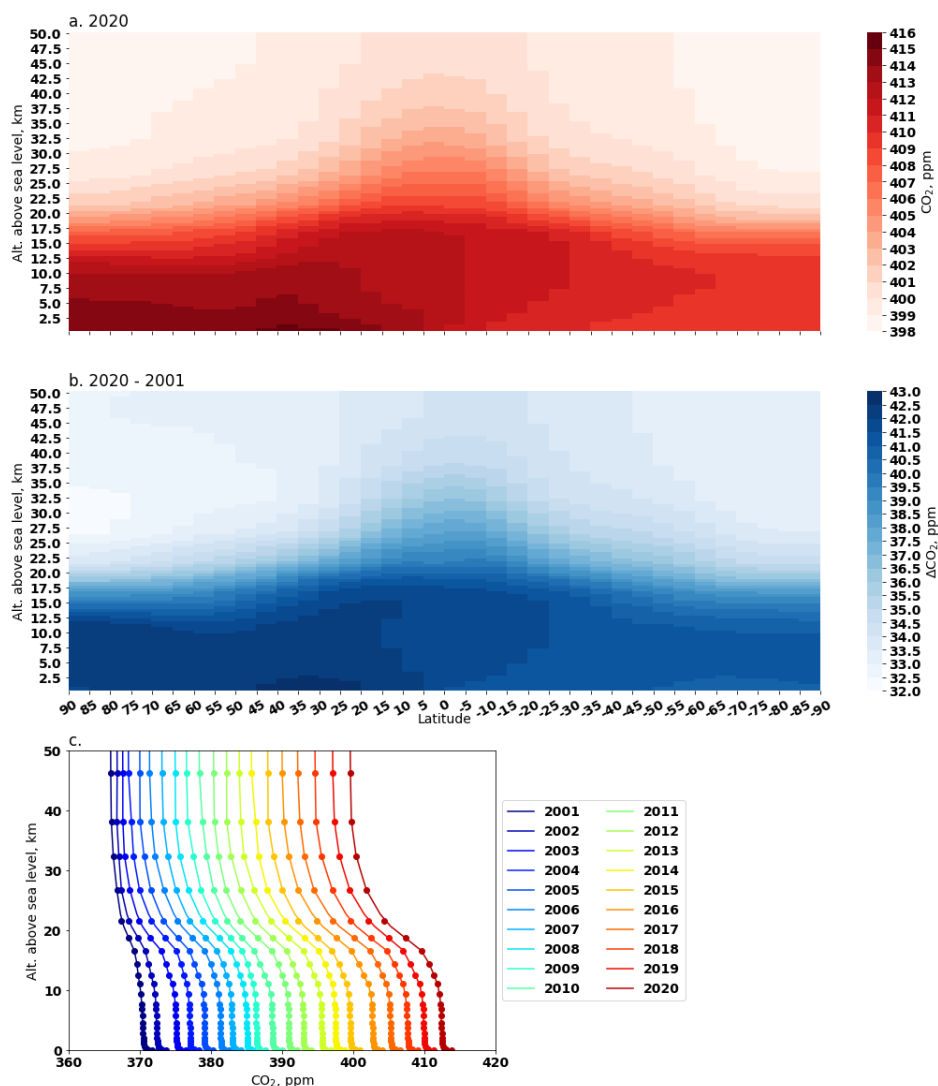
270

271   **Figure 6. Global vertical profile of CO₂ mole fraction derived from CTE model output. Panel (a) shows the vertical**
272   **profile in 2020. Panel (b) shows the difference of the vertical profile between 2001 and 2020. Panel (c) shows the annual**
273   **mean vertical profile from 2001 to 2020, the dots mark CTE vertical level heights and lines are the linear interpolation**
274   **between the heights.**

275   The CTE model simulates CO₂ mole fraction over a global 3D grid, which allows us to view the modelled vertical CO₂ profile.

276   In the lower atmosphere, highest CO₂ mole fraction are found in the Northern mid-latitude (dark red between 30 ºN and 40

277   ºN, Fig. 6a), where more anthropogenic emissions take place, which are subsequently transported towards northern and

278   southern latitudes. The latitudinal and interhemispheric gradient of atmospheric CO₂ found in Fig. 6a, is not only determined

279   by the latitudinal and interhemispheric differences in fossil fuel emissions and seasonal exchange with terrestrial biota

280   (Denning et al., 1995), but is also due to atmospheric transport (Patra et al., 2011). With increasing altitude, the gradient

281   between Northern and Southern hemisphere becomes small and levels out at higher altitudes (e.g. >50 km). When comparing

282   the vertical profile change between 2001 and 2020 (Fig. 6b and 6c), the CO_2 mole fraction increases slower at the higher

283   atmosphere (>25 km altitude) than the increase at the lower atmosphere (<25 km altitude). Fig. 6c shows that the vertical

284   gradient (difference between 50 km and 0.05 km) changes from ~5 ppm for 2001 to ~13 ppm for 2020. The high vertical

285   gradient in 2020 reflects the accumulation of CO_2 in the lower atmosphere, which is caused by continuous CO_2 emissions

286   from the surface during 2001-2020 and slow vertical transport. The low vertical gradient in 2001 is partly due to low surface

287   emission.

288   **3.3 Relationship between the surface CO_2 mole fraction and atmospheric CO_2 mass**
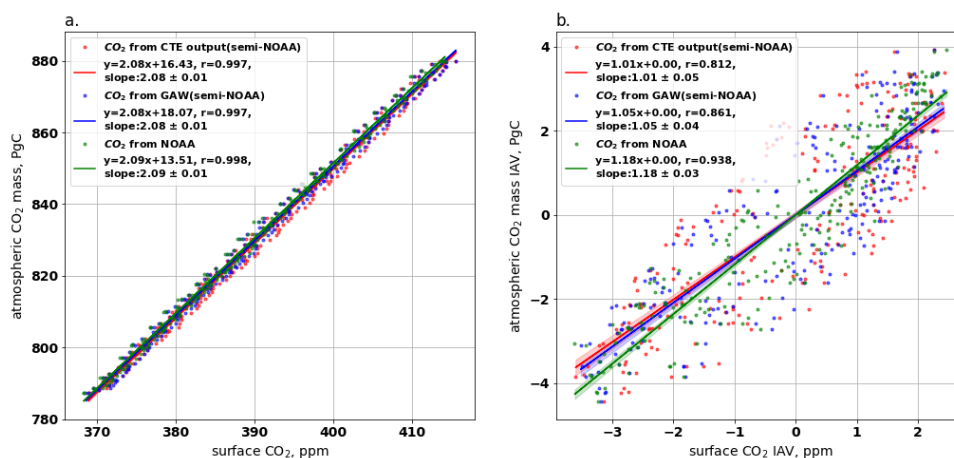
289

290   **Figure 7. Relationship between the monthly surface CO_2 mole fraction and atmospheric CO_2 mass. The atmospheric**
291   **CO_2 mass calculated from the 3D CTE output. In panel (a), the monthly surface CO_2 derived from the CTE_output**
292   **(semi-NOAA), GAW (semi-NOAA) and NOAA analysis, presented as blue, red and green dots, respectively. Panel (b)**
293   **compare the corresponding interannual variability (IAV) of the atmospheric CO_2 mass and the surface CO_2. The IAV**
294   **is calculated as the anomaly departure from a quadratic trend.**

295   Atmospheric CO_2 mass calculated from the CTE output as a function of air mass and CO_2 concentration (Text S3), has

296   increased from 789.46 PgC in 2001 to 877.88 PgC in 2020 (Fig. S3a). The spatial distribution of the atmospheric CO_2 mass

297   can be seen in Fig. S3b and Fig. S3c. Monthly global surface CO_2 mole fraction derived from CTE output (red dots, Fig. 7a)

298   at the 230 sites used in CTE with the semi-NOAA method (CTE_output (semi-NOAA)) and GAW observations (blue dots,

299   Fig. 7a) at 139 GAW sites with the semi-NOAA method (GAW (semi-NOAA)) has a similar linear relationship (showing the

300   same slope of 2.08±0.01 PgC ppm^{-1}) as the monthly atmospheric CO_2 total mass derived from the CTE output. The NOAA

301   CO_2 (green dots, Fig. 7a) shows a similar linear relationship (has a slope of 2.09±0.01 PgC ppm^{-1}). The slope or conversion

302   factor in Fig. 7a is slightly lower than the factor 2.12 PgC ppm^{-1} used in Ballantyne et al. (2012) for the period 1980-2010.

303   The small difference in conversion factor is expected, considering the different model and data used. We further compare the

304   interannual variability (IAV, calculated as the anomaly departure from a quadratic trend) of the atmospheric CO_2 mass and

305   the surface CO_2 (Fig. 7b), the coefficient of the linear relationship is very close to ~1.0, which indicates the temporal change

306   in atmospheric CO_2 mass agrees with temporal change in surface CO_2 mole fraction. The NOAA network tracks atmospheric

307   CO_2 change slightly better (r=0.938) than the GAW (r=0.861) and CTE (r=0.812) networks, given the long resident time and

308   well-mixed nature of atmospheric CO_2. Overall, the relationship found in Fig. 7 implies that the current surface CO_2 network

309   can be a good indicator of the CO_2 mass change in the whole atmosphere through a linear relationship.

3.4 Annual absolute change and interannual variability of global CO_2 mole fraction
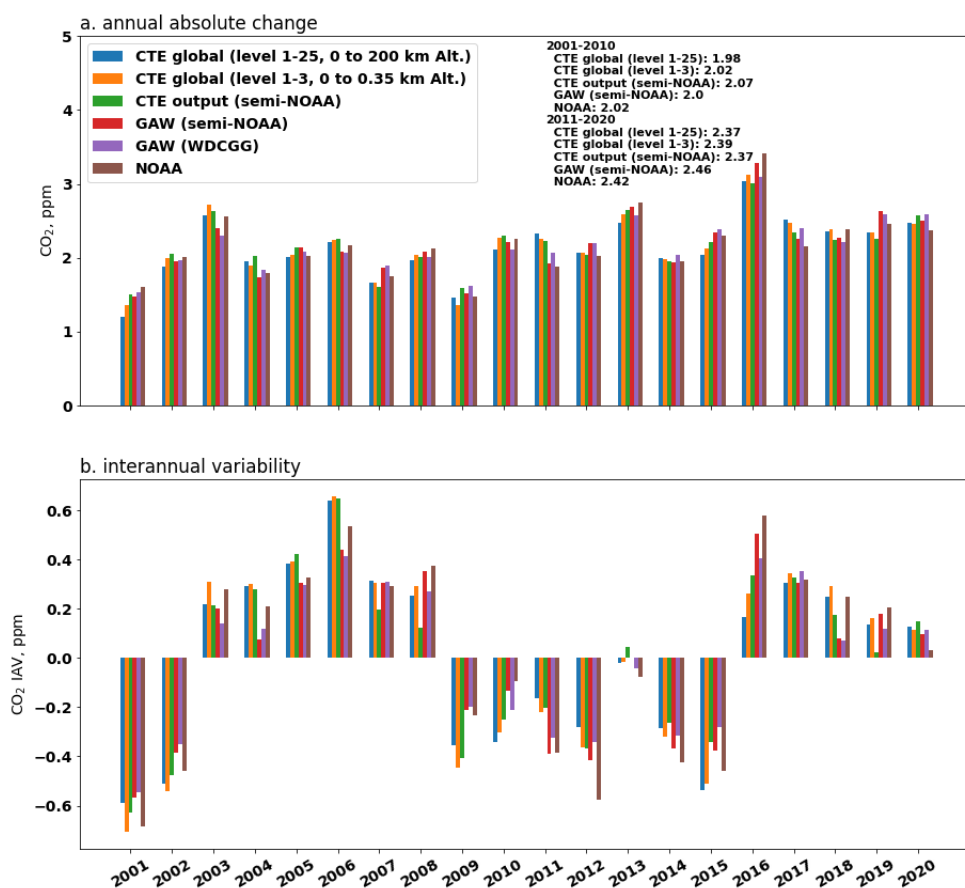
Figure 8. Annual absolute change and interannual variability of global CO_2 mole fraction derived from different data (CTE model, GAW observation and NOAA observation) and analysis methods (semi-NOAA method, WDCGG method and NOAA method) for 2000-2020. Panel (a) shows the annual absolute change which is the difference between annal mean. Averages over 2001-2010 and 2011-2020 are also shown. Panel (b) shows the IAV which is calculated as the anomaly departure from a quadratic trend.

Pressure-weighted average CO_2 in the lower atmosphere and whole atmosphere is derived from CTE output. The annual absolute change (calculated as the difference between annual mean) of CO_2 in the lower atmosphere (0 to 0.35 km altitude, orange bars in Fig. 8a) is more sensitive to surface sink and source than the change in the whole atmosphere (blue bars). The reason is that the whole atmosphere has a larger air volume than the lower atmosphere, and the change of the surface CO_2 is diluted due to horizontal and vertical transport. The CO_2 change derived from the observations of the GAW network (red bars for semi-NOAA method, purple bars for WDCGG method) and the NOAA network (brown bars), shows a small positive or negative difference from the CTE results over the different years. However, over the long term (e.g. decadal scale, 2001-2010 and 2011-2020), the CTE model derived change of lower and whole atmospheric CO_2 shows good agreement (<0.09 ppm yr^{-1}) with the surface observation-based estimate, especially for the lower atmospheric CO_2 (<0.07 ppm yr^{-1}). Fig. 8b shows the IVA derived from CTE (blue, orange and green bars) follows a similar temporal pattern as the observation-based IVA derived

327   from the GAW and NOAA network (red, purple and brown bars), especially the IVA of the low-level atmosphere (orange

328   bars) show good agreement with the observation-based IVA (r>0.971, RMSE<0.178 ppm).

4 Discussion

330   During the past few decades, observational networks have been extended (e.g. from the NOAA MBL network) to the

331   continents (e.g. GAW network and CTE network, Fig. 1) in order to monitor global CO_2 concentrations and quantify CO_2

332   sources and sinks. Although the continental observations include contributions from both big sources of anthropogenic

333   emissions and big sources/sinks from terrestrial vegetation off/during the growing season, these continental observations show

334   an overall higher global surface CO_2 mole fraction in the global CO_2 analysis which indicates that they are influenced by a

335   net source. We find that the global mean derived from the GAW network is on average 0.329 (semi-NOAA method) or 0.336

336   (WDCGG method) ppm consistently higher than that derived from the NOAA network during 1980-2020, similarly ~0.350

337   ppm higher mole fraction in the GAW network was found in Tsutsumi et al. (2009) for 1983-2006. The CTE network even

338   leads to a higher global mean (0.422 ppm during 1980-2020), which is likely due to more observational sites locate in the

339   Northern Hemisphere where the highest anthropogenic emissions take place. This also explains the large fluctuation of CO_2

340   concentration during the winters and summers during 2001-2020 (green and orange lines, Fig. 4a). In future, we expect that

341   adding new observation sites (specially in Northern Hemisphere) into the current observational network (e.g. GAW network),

342   would lead to higher global surface CO_2 and a larger amplitude of the global CO_2 seasonal cycle in the global CO_2 analysis.

343   Although Friedlingstein et al. (2022) reported a 5.4% drop (~0.52 PgC) in fossil fuel CO_2 emissions in 2020 (due to restrictions

344   on e.g. transport, industry, power etc during the COVID-19 pandemic), the increase in annual CO_2 from 2019 to 2020

345   (2.60±0.16 ppm yr^{-1}) remains at a similar level as from 2018 to 2019 (2.61±0.05 ppm yr^{-1}). In principle, an equivalent drop of

346   roughly 0.25 ppm yr^{-1} (according to the conversion factor 2.08 PgC ppm^{-1} in Fig. 7a) or roughly 0.13 ppm yr^{-1} (according to

347   the annual absolute change, red bars in Fig. 8a) in the growth rate should be visible for period 2019-2020 due to the declined

348   CO_2 emission. However, such short-term human activity induced change of the CO_2 growth rate may be hidden by the natural

349   variability. The bootstrap analysis is used in this study (also in Conway et al., (1994) and Tsutsumi et al., (2009)) to estimate

350   the uncertainty of the CO_2 temporal mean and its growth rate and to assess how sensitive the global value is to the distribution

351   of sampling sites. The relatively large uncertainty (±0.16 ppm yr^{-1}) at the end of 2020 compared to previous years (Table 1)

352   is likely due to end-effect associated with the curve fitting and filter procedure. The end-effect is a tendency for the growth

353   rate to turn toward the mean value at the end of the record (Conway et al., 1994), therefore Conway et al. (1994) suggested

354   the last 6 months of the growth rate curves should be viewed with caution.

355   Our analysis shows that basing the CO_2 growth rate on GAW surface observations does not introduce a large bias (on average

356   agreement within 0.015 ppm yr^{-1}) compared to a full atmospheric analysis (Fig. 4b and 8, Table S1e-f). This full atmosphere

357   CO_2 was provided by the CTE model, in which the global annual mean CO_2 is significantly overestimated compared to GAW

358   observations (e.g. 0.299 ppm higher in CTE_output (semi-NOA), or 0.186 ppm higher in the CTE_global (semi-NOAA)

359   during 2001-2020). The overestimate derived from the CTE_output (semi-NOAA), i.e. CTE outputs at the CTE 230 sites, is

360   mainly due to more sites in the Northern Hemisphere in the CTE network than in the GAW network. The lower overestimate

361   derived from the CTE_global (semi-NOAA), i.e. CTE outputs at full global grids at the low-level atmosphere, implies that

362   the biases in CTE are not uniform spatially and attempt to balance out. We estimate the CTE bias by comparing the

363   observations and CTE outputs at the same sites, which results in 0.069 ppm low bias derived from the CTE outputs in

364   calculating the global surface CO_2 mole fraction.

365   Different observational networks (i.e. NOAA network, GAW network and CTE network) are analysed in this study, which

366   shows a difference in calculated global surface CO_2 mole fractions equivalent to the current atmospheric growth rate over a

367   three-month period. This implies that the station selection, especially if and how many continental observations are used, has

368   some but not a particularly strong influence on the derived global surface CO_2. Nowadays more and more continental

369   observations are established in order to monitor biogenic sources and sinks, and further provide insight into the climate change

370   and the associated ecosystem processes (Ciais et al., 2005, Ramonet et al., 2020). Such continental observations carry more

371   variability in measurements than the marine observations, which needs some caution when used in the mix of stations for

372   determining global surface CO_2 mole fraction. However, our study shows that continental sites can help early detect the change

373   of CO_2 growth rate caused by biogenic emission change (e.g. caused by El Niño events). Besides, current observational

374   networks (with and without continental sites) and CTE model show a good agreement within 0.025 ppm yr^{-1} on the global

375   CO_2 growth rate over long-term period. This implies that the current observation networks (e.g. as shown in Fig. 1, represent

376   for multiple ecosystems, multiple sinks and sources, and different latitudes) have a similar good capacity to capture the global

377   surface CO_2 changes, although there is the spatial and temporal variability of the CO_2 growth rate (e.g. Conway et al. 1994).

378   We also notice that the uncertainty global CO_2 growth rate is approximately 0.07 ppm yr^{-1}, as derived from GAW (semi-

379   NOAA) and averaged over 1980-2020 (Table 1). In order to reduce this uncertainty, we recommend adding more stations to

380   the current observation network. We conducted an experiment (Fig. S4) which demonstrates that the uncertainty of the global

381   CO_2 growth rate exponentially increases as the number of land observation sites is reduced. To reduce the uncertainty to 0.02

382   ppm yr^{-1} (equivalent to 1% of the global CO_2 growth rate), our experiment indicates that 332 land observation sites are required

383   (Fig. S4). However, the required number of sites also depends on their geographical distribution (i.e. CO_2 footprint coverage

384   of observation network, and the importance of the network design was addressed by Storm et al. (2022)), measurement

385   accuracy, and consistency.

386   Extrapolation beyond the measurement period extends knowledge gained from a limited period of measurements. During a

387   limited period of measurement, we can define the average seasonality, long-term trend, and short-term variation at a

388   measurement site. The long-term trend of individual site is extrapolated, for example by referring to the latitude reference

389   time series (Masarie and Tans, 1995) or the mean long-term trend over sites within a certain (e.g. 30°) latitudinal zone

390   (Tsutsumi et al., 2009), and then combining the extrapolated trend with average seasonality to produce the estimate beyond

391   measurement period. The extrapolation requires the assumption that the relationship of an individual site to the latitude

392   reference is invariant in time, however, the relationship between nearby sites is continuously changing (Masarie and Tans,

393   1995). Besides, the short-term variation is ignored or estimated from nearby sites, which introduces extra uncertainty from

394   extrapolation. In this study, we find that the WDCGG method with extrapolation (GAW (WDCGG+)) results in ~0.096 ppm

395   higher in the global surface CO_2 mole fraction than the WDCGG method without extrapolation (GAW (WDCGG)) using the

396   same GAW observations, although the extrapolation has a tiny effect on the growth rate (Table S2). Therefore, extrapolation

397   beyond the measurement period is not used in our analysis. With the increasing number of long-term measurements, this

398   extrapolation becomes less and less necessary.

399   **5 Conclusions**

400   The WMO Global Atmosphere Watch CO_2 network documents the gradual global accumulation of CO_2 in the atmosphere

401   due to human activities, and has been used to assess large-scale and long-term environmental consequence of fossil CO_2

402   emission and land use changes. Although the current CO_2 network is sparse due to operational costs and logistical constraints,

403   it has a good capacity to represent global surface CO_2 mole fraction and its growth rate and trends in atmospheric CO_2 mass

404 changes. The three different analysis methods yield very similar global CO_2 increase from 2001 to 2020, which gives

405 confidence to use either one of them in climate change study. The continuous monitoring the atmospheric CO_2, basing on the

406 current GAW network together with reliable global data integration methods, provides essential information for policymakers

407 to support their efforts in mitigating the global warming.

6 Data and Code Availability

409 All data and code necessary to calculate the global mean surface CO_2 mole fraction and Atmospheric CO_2 mass is freely

410 available from ICOS Carbon Portal [https://doi.org/10.18160/Q788-9081]. The file list of results and code can be found in

411 Text S4.

Acknowledgments

413 We acknowledge Ingrid Luijkx for providing the TM5 data, WMO GAW Principal Investigators of the WMO GAW station

414 network for providing the observational data, Ed Dlugokencky for providing NOAA data and comments. Thanks to the support

415 from ICOS, GAW, NOAA and CTE group.

Author Contributions

417 A.V. and Z.W. designed this study in discussion with Y.S., O.T and U.K..

418 Z.W. performed analysis and led the writing.

419 Y.S., Y.N. and A.O. provided the GAW data, and commented on the manuscript.

420 W.P. and R.K. provided CTE model results and relevant ObsPack data, and commented on the manuscript.

421 X.L. provided NOAA data and commented on the manuscript.

422 All authors contributed to the writing of the paper and interpretation of the results.

Competing Interests

424 The authors declare no competing interests.

425

Financial support

427 This research is a part of ICOS core work, there is no grant reference no.

References

429 BALLANTYNE, A. Á., ALDEN, C. Á., MILLER, J. Á., TANS, P. Á. & WHITE, J. 2012. Increase in observed net carbon dioxide uptake
430   by land and oceans during the past 50 years. *Nature,* 488**,** 70-72. https://doi.org/10.1038/nature11299
431 CIAIS, P., REICHSTEIN, M., VIOVY, N., GRANIER, A., OGÉE, J., ALLARD, V., AUBINET, M., BUCHMANN, N., BERNHOFER,
432   C. & CARRARA, A. 2005. Europe-wide reduction in primary productivity caused by the heat and drought in 2003. *Nature,* 437**,**
433   529-533. https://doi.org/10.1038/nature03972
434 CONWAY, T. J., TANS, P. P., WATERMAN, L. S., THONING, K. W., KITZIS, D. R., MASARIE, K. A. & ZHANG, N. 1994. Evidence
435   for interannual variability of the carbon cycle from the National Oceanic and Atmospheric Administration/Climate Monitoring
436   and Diagnostics Laboratory global air sampling network. *Journal of Geophysical Research: Atmospheres,* 99**,** 22831-22855.
437   https://doi.org/10.1029/94JD01951
438 DENNING, A. S., FUNG, I. Y. & RANDALL, D. 1995. Latitudinal gradient of atmospheric CO2 due to seasonal exchange with land biota.
439   *Nature,* 376**,** 240-243. https://doi.org/10.1038/376240a0

440 EYRING, V., GILLETT, K., ACHUTA RAO, R., BARIMALALA, M., BARREIRO PARRILLO, N., BELLOUIN, C., CASSOU, P.,
441   DURACK, Y., KOSAKA, S. & MCGREGOR, S. 2021. Human Influence on the Climate System. *Climate Change 2021: The*
442   *Physical Science Basis. Contribution of Working Group I to the Sixth Assessment Report of the Intergovernmental Panel on*
443   *Climate Change.* https://www.ipcc.ch/report/ar6/wg1/
444 FRIEDLINGSTEIN, P., JONES, M. W., O'SULLIVAN, M., ANDREW, R. M., BAKKER, D. C., HAUCK, J., LE QUÉRÉ, C., PETERS,
445   G. P., PETERS, W. & PONGRATZ, J. 2022. Global carbon budget 2021. *Earth System Science Data,* 14, 1917-2005.
446   https://doi.org/10.5194/essd-14-1917-2022
447 GULEV, S., THORNE, P., AHN, J., DENTENER, F., DOMINGUES, C. M., GONG, S. G. D., KAUFMAN, D., NNAMCHI, H., RIVERA,
448   J. & SATHYENDRANATH, S. 2021. Changing state of the climate system. *Climate Change 2021: The Physical Science Basis.*
449   *Contribution of Working Group I to the Sixth Assessment Report of the Intergovernmental Panel on Climate Change.*
450   https://www.ipcc.ch/report/ar6/wg1/
451 HALL, B. D., CROTWELL, A. M., KITZIS, D. R., MEFFORD, T., MILLER, B. R., SCHIBIG, M. F. & TANS, P. P. 2021. Revision of
452   the World Meteorological Organization Global Atmosphere Watch (WMO/GAW) CO 2 calibration scale. *Atmospheric*
453   *Measurement Techniques,* 14, 3015-3032. https://doi.org/10.5194/amt-14-3015-2021
454 SCHULDT, K.N., et al. 2022. Multi-laboratory compilation of atmospheric carbon dioxide data for the period 1957-2021. *NOAA Earth*
455   *System Research Laboratory, Global Monitoring Laboratory.* http://doi.org/10.25925/20220808
456 KROL, M., DE BRUINE, M., KILLAARS, L., OUWERSLOOT, H., POZZER, A., YIN, Y., CHEVALLIER, F., BOUSQUET, P., PATRA,
457   P. & BELIKOV, D. 2018. Age of air as a diagnostic for transport timescales in global models. *Geoscientific Model Development,*
458   11, 3109-3130. https://doi.org/10.5194/gmd-11-3109-2018
459 KROL, M., HOUWELING, S., BREGMAN, B., VAN DEN BROEK, M., SEGERS, A., VAN VELTHOVEN, P., PETERS, W.,
460   DENTENER, F. & BERGAMASCHI, P. 2005. The two-way nested global chemistry-transport zoom model TM5: algorithm and
461   applications. *Atmospheric Chemistry and Physics,* 5, 417-432. https://doi.org/10.5194/acp-5-417-2005
462 LÜTHI, D., LE FLOCH, M., BEREITER, B., BLUNIER, T., BARNOLA, J.-M., SIEGENTHALER, U., RAYNAUD, D., JOUZEL, J.,
463   FISCHER, H. & KAWAMURA, K. 2008. High-resolution carbon dioxide concentration record 650,000–800,000 years before
464   present. *nature,* 453, 379-382. http://doi.org/10.1038/nature06949
465 MASARIE, K. A. & TANS, P. P. 1995. Extension and integration of atmospheric carbon dioxide data into a globally consistent measurement
466   record. *Journal of Geophysical Research: Atmospheres,* 100, 11593-11610. https://doi.org/10.1029/95JD00859
467 PATRA, P. K., HOUWELING, S., KROL, M., BOUSQUET, P., BELIKOV, D., BERGMANN, D., BIAN, H., CAMERON-SMITH, P.,
468   CHIPPERFIELD, M. P. & CORBIN, K. 2011. TransCom model simulations of CH 4 and related species: linking transport, surface
469   flux and chemical loss with CH 4 variability in the troposphere and lower stratosphere. *Atmospheric Chemistry and Physics,* 11,
470   12813-12837. https://doi.org/10.5194/acp-11-12813-2011
471 PETERS, W., KROL, M., DLUGOKENCKY, E., DENTENER, F., BERGAMASCHI, P., DUTTON, G., VELTHOVEN, P. V., MILLER,
472   J., BRUHWILER, L. & TANS, P. 2004. Toward regional-scale modeling using the two-way nested global model TM5:
473   Characterization of transport using SF6. *Journal of Geophysical Research: Atmospheres,* 109.
474   https://doi.org/10.1029/2004JD005020
475 PRESS, W. H., TEUKOLSKY, S. A., VETTERLING, W. T. & FLANNERY, B. P. 1988. *Numerical recipes in C 1st edition: The art of*
476   *scientific computing,* Cambridge university press.
477   https://citeseerx.ist.psu.edu/document?repid=rep1&type=pdf&doi=e05e217a58481314e070b6c8899791faa91a3e27
478 RAMONET, M., CIAIS, P., APADULA, F., BARTYZEL, J., BASTOS, A., BERGAMASCHI, P., BLANC, P., BRUNNER, D.,
479   CARACCIOLO DI TORCHIAROLO, L. & CALZOLARI, F. 2020. The fingerprint of the summer 2018 drought in Europe on
480   ground-based atmospheric CO2 measurements. *Philosophical Transactions of the Royal Society B,* 375, 20190513.
481   https://doi.org/10.1098/rstb.2019.0513
482 SARMIENTO, J. L., GLOOR, M., GRUBER, N., BEAULIEU, C., JACOBSON, A. R., MIKALOFF FLETCHER, S. E., PACALA, S. &
483   RODGERS, K. 2010. Trends and regional distributions of land and ocean carbon sinks. *Biogeosciences,* 7, 2351-2367.
484   https://doi.org/10.5194/bg-7-2351-2010
485 STORM, I., KARSTENS, U., D'ONOFRIO, C., VERMEULEN, A. & PETERS, W. 2022. A view of the European carbon flux landscape
486   through the lens of the ICOS atmospheric observation network. *Atmospheric Chemistry and Physics Discussions,* 1-25.
487   https://doi.org/10.5194/acp-23-4993-2023
488 TANS, P. P., THONING, K. W., ELLIOTT, W. P. & CONWAY, T. J. 1990. Error estimates of background atmospheric CO2 patterns from
489   weekly flask samples. *Journal of Geophysical Research: Atmospheres,* 95, 14063-14070.
490   https://doi.org/10.1029/JD095iD09p14063
491 THONING, K. W., TANS, P. P. & KOMHYR, W. D. 1989. Atmospheric carbon dioxide at Mauna Loa Observatory: 2. Analysis of the
492   NOAA GMCC data, 1974–1985. *Journal of Geophysical Research: Atmospheres,* 94, 8549-8565.
493   https://doi.org/10.1029/JD094iD06p08549
494 TSUTSUMI, Y., MORI, K., HIRAHARA, T., IKEGAMI, M. & CONWAY, T. J. 2009. Technical Report of Global Analysis Method for
495   Major Greenhouse Gases by the World Data Center for Greenhouse Gases (WMO/TD-No. 1473). *GAW Report No. 184. Geneva,*
496   *WMO,*, 1-23. https://library.wmo.int/index.php?lvl=notice_display&id=12631
497 VAN DER LAAN-LUIJKX, I. T., VAN DER VELDE, I. R., VAN DER VEEN, E., TSURUTA, A., STANISLAWSKA, K.,
498   BABENHAUSERHEIDE, A., ZHANG, H. F., LIU, Y., HE, W. & CHEN, H. 2017. The CarbonTracker Data Assimilation Shell
499   (CTDAS) v1. 0: implementation and global carbon balance 2001–2015. *Geoscientific Model Development,* 10, 2785-2800.
500   https://doi.org/10.5194/gmd-10-2785-2017
501 WMO, G. 2022. The state of greenhouse gases in the atmosphere based on global observations through 2021. *WMO Greenhouse Gas*
502   *Bulletin.* https://library.wmo.int/doc_num.php?explnum_id=11352
503

504